

ChimeraLM detects amplification artifacts for  
accurate structural variant calling in long-read  
single-cell sequencing

Yangyang Li<sup>1†</sup>, Qingxiang Guo<sup>1†</sup>, Rendong Yang<sup>1,2\*</sup>

<sup>1</sup>Department of Urology, Northwestern University Feinberg School of Medicine, 303 E Superior St, Chicago, 60611, IL, USA.

<sup>2</sup>Robert H. Lurie Comprehensive Cancer Center, Northwestern University Feinberg School of Medicine, 675 N St Clair St, Chicago, 60611, IL, USA.

\*Corresponding author(s). E-mail(s): [rendong.yang@northwestern.edu](mailto:rendong.yang@northwestern.edu);  
Contributing authors: [yangyang.li@northwestern.edu](mailto:yangyang.li@northwestern.edu);

[qingxiang.guo@northwestern.edu](mailto:qingxiang.guo@northwestern.edu);

†These authors contributed equally to this work.

### Abstract

Single-cell genomics enables unprecedented cellular heterogeneity insights but faces a fundamental challenge: Whole Genome Amplification (WGA) introduces chimeric artifacts that generate false Structural Variations (SVs), undermining biological interpretations. Current computational methods cannot distinguish amplification-induced artifacts from genuine rearrangements. Here we present ChimeraLM, a genomic language model that learns sequence-level features discriminating biological sequences from WGA artifacts. Validated on nanopore data, ChimeraLM achieves 95% recall with 70% precision and reduces chimeric content by ~90% while preserving 72–92% of true SVs. This improves SV validation rates 8–11 fold and eliminates false-positive inversion (INV) bias, restoring SV distributions to bulk-like profiles. Attention visualization reveals ChimeraLM focuses on junction regions with single-base precision, learning interpretable features applicable across sequencing technologies. By enabling confident SV detection at single-cell resolution, ChimeraLM addresses a fundamental data quality barrier in cancer genomics, developmental biology, and precision medicine. Available at <https://github.com/ylab-hi/ChimeraLM>.

**Keywords:** Whole Genome Amplification, Single Cell, Genomic Language Model, Structural Variation

047 **Main**

048

049 Single-cell genomics has revolutionized our understanding of cellular heterogeneity  
050 by enabling characterization of individual cells rather than bulk populations [1–4],  
051 revealing previously hidden biological complexity. This approach has proven instru-  
052 mental in uncovering rare cell types [4], tracking developmental trajectories [3], and  
053 elucidating tumor evolution through clonal architecture analysis. However, the limited  
054 DNA content in a single cell—typically only 6–7 picograms containing approximately  
055 two copies of the 3-billion-base-pair human genome—poses significant technical chal-  
056 lenges for comprehensive genomic analysis [5–7]. To overcome this limitation, **WGA**  
057 has become essential for single-cell genomic studies [4, 7–10]. Various **WGA** techniques  
058 have been developed, each with distinct amplification mechanisms and characteris-  
059 tic error profiles. **Multiple Displacement Amplification (MDA)**, introduced by Dean  
060 et al. [10], utilizes the highly processive phi29 DNA polymerase to achieve isother-  
061 mal amplification with products exceeding 10 kb, though it suffers from pronounced  
062 amplification bias and chimera formation [11, 12]. **Degenerate Oligonucleotide-Primed**  
063 **PCR (DOP-PCR)**, pioneered by Telenius et al. [13], employs thermocycling with  
064 degenerate primers to achieve more uniform coverage but generates shorter amplicons.  
065 **Multiple Annealing and Looping-based Amplification Cycles (MALBAC)** combines  
066 quasi-linear preamplification with exponential amplification to reduce bias [8], while  
067 **Linear Amplification via Transposon Insertion (LIANTI)** uses transposon insertion  
068 to create defined amplification origins, significantly improving uniformity and reduc-  
069 ing artifacts [7]. More recently, **Primary Template-directed Amplification (PTA)** [14]  
070 and **droplet-based MDA (dMDA)** [15, 16] have emerged as promising alternatives  
071 that modify reaction conditions to suppress chimera formation, though these meth-  
072 ods require specialized equipment and protocols that have limited their widespread  
073 adoption. These amplification methods can increase DNA content by several orders  
074 of magnitude (typically 1,000- to 10,000-fold), generating sufficient material for high-  
075 coverage sequencing necessary for reliable variant calling, copy number analysis, and  
076 **SV** detection [4, 17–21].

077 Accurate single-cell genomics is particularly critical for multiple applications where  
078 false-positive **SVs** can lead to incorrect biological conclusions. In cancer research, dis-  
079 tinguishing genuine clonal evolution patterns from amplification artifacts is essential  
080 for understanding tumor heterogeneity and therapeutic resistance [3]. In develop-  
081 mental biology, accurate detection of somatic mosaicism enables the reconstruc-  
082 tion of lineage relationships and identification of pathogenic mutations in rare cell pop-  
083 ulations. For CRISPR-based genome editing, single-cell analysis with reliable **SV**  
084 detection is crucial for comprehensive assessment of off-target effects and ensuring  
085 genomic stability [14]. However, false-positive **SVs** introduced during amplification can  
086 confound these analyses, leading to misinterpretation of genomic rearrangements and  
087 their biological significance [4, 22].

088 Despite its critical role, **WGA** introduces systematic artifacts that significantly  
089 impact downstream analyses [7, 11, 12, 22, 23]. Chief among these are chimeric  
090 sequences—artificial DNA constructs formed through template switching during  
091 amplification, which can comprise 42–76% of long-read sequencing data [22]. Dur-  
092 ing **MDA**, the highly processive phi29 polymerase can dissociate from one genomic

template and reinitiate synthesis on another, creating chimeric molecules that join DNA fragments from distant genomic loci into single amplified products [11]. These artifacts are particularly problematic for long-read sequencing technologies, where chimeric reads can span tens of kilobases and generate false-positive <b>SVs</b> that are indistinguishable from genuine genomic rearrangements by current computational methods.	093
Current computational tools to detect <b>SVs</b> from long-read data, including Sniffles2 [24, 25], DeBreak [26], SVIM [27], and cuteSV [28]. These methods typically employ read alignment analysis, split-read detection, and local assembly strategies to identify <b>SV</b> signatures [29]. However, distinguishing genuine biological <b>SVs</b> from <b>WGA</b> -induced chimeric artifacts remains challenging [23, 30–32].	099
Current computational approaches for identifying <b>WGA</b> -induced artifacts rely primarily on coverage-based metrics and read-pair orientation patterns [23, 30]. However, these heuristic methods often fail to distinguish genuine <b>SVs</b> from amplification artifacts, particularly when chimeric sequences exhibit complex rearrangement patterns, occur in repetitive genomic regions, or involve multiple genomic loci [31, 32]. This lack of robust, automated artifact detection has limited the reliability of <b>SV</b> analysis in single-cell studies and hindered the full realization of single-cell genomics' potential for studying somatic mosaicism, tumor evolution, and rare cell populations.	104
The emergence of deep learning, particularly language models based on transformer architectures, has demonstrated remarkable success in genomics applications [33–36]. Recent genomic language models have shown the ability to learn complex sequence patterns and contextual relationships in DNA sequences, enabling improved performance in tasks such as regulatory element prediction, variant effect prediction, and functional annotation [36–38]. These models treat DNA sequences analogously to natural language, learning representations that capture both local motifs and long-range dependencies [33]. By training on large-scale genomic datasets, such models can internalize patterns of genuine biological sequences, including characteristic features of repetitive elements, chromatin structure, and sequence composition biases.	112
Here, we developed ChimeraLM, a platform-agnostic genomic language model specifically designed to detect chimeric artifacts introduced by <b>WGA</b> . Unlike existing heuristic methods that rely on platform-specific coverage or orientation patterns, ChimeraLM learns sequence-level features that are universal across sequencing technologies. By leveraging deep learning to capture sequence patterns, structural features, and contextual information in genomic reads [33–36, 38], ChimeraLM effectively distinguishes genuine biological sequences from <b>WGA</b> -induced chimeric artifacts. We demonstrate that ChimeraLM achieves superior performance compared to existing methods and substantially improves the reliability of <b>SV</b> detection in single-cell genomic studies, thereby enabling accurate SV analysis at single-cell resolution.	122
<b>Results</b>	133
<b>Overview of ChimeraLM workflow and model architecture</b>	135
Single-cell genomics relies on <b>WGA</b> to obtain sufficient DNA for sequencing (Fig. 1a). The standard workflow includes single-cell isolation, DNA extraction, <b>WGA</b> , long-read	136
	137
	138

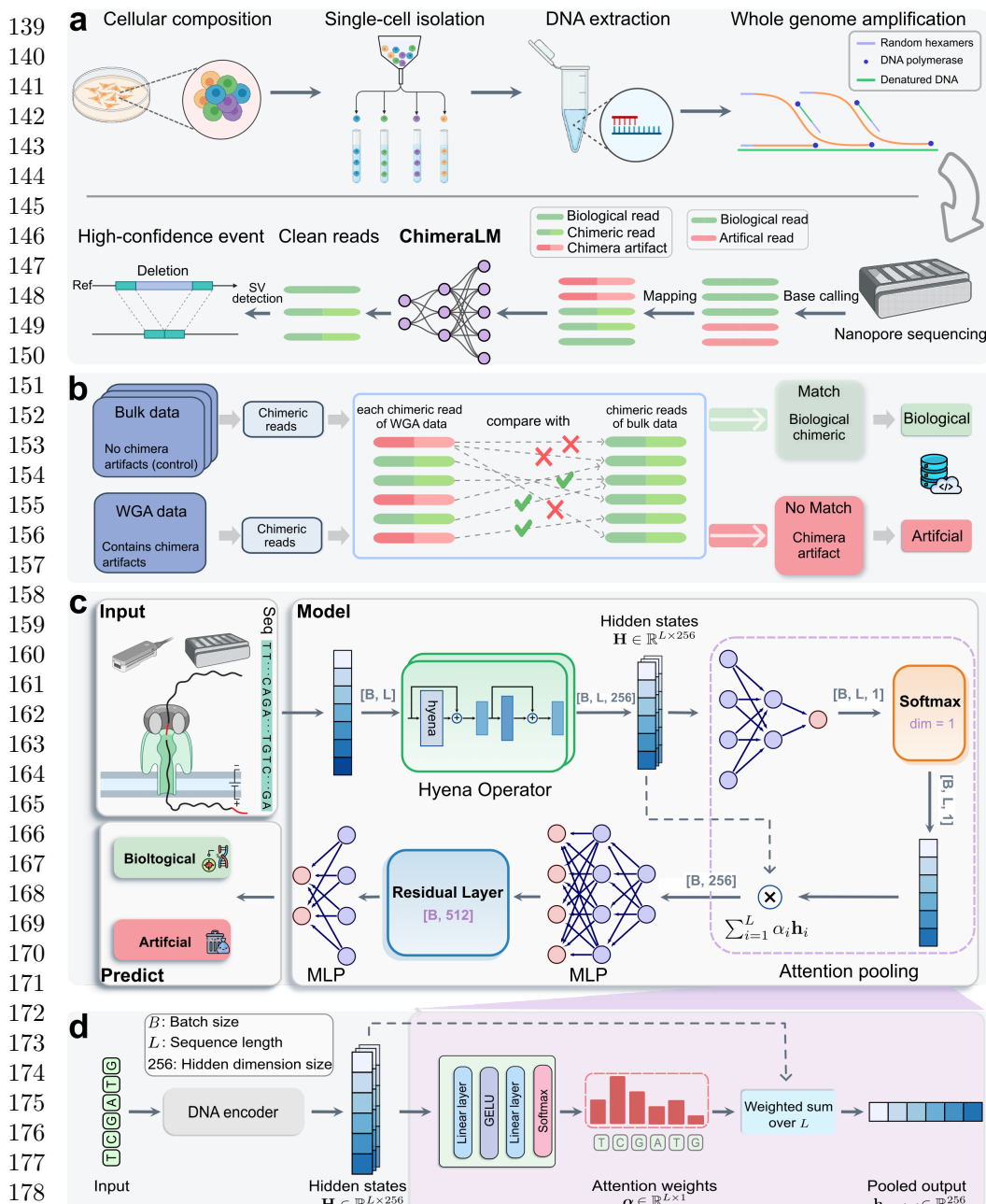


**Fig. 1 ChimeraLM workflow and architecture for detecting WGA artifacts in single-cell sequencing.** (a) Single-cell genomic workflow and ChimeraLM integration. Single cells are isolated, followed by DNA extraction and WGA for genome amplification. WGA generates chimeric artifacts (red) through template switching during amplification, alongside biological reads (green). After nanopore sequencing, ChimeraLM classifies chimeric reads as biological or artificial, enabling downstream SV detection on clean reads. (b) Ground truth label generation for supervised learning. Chimeric reads from WGA data are compared against all chimeric reads from bulk sequencing data of the same cell line. Reads that match bulk data are labeled as biological (green pathway), while non-matching reads are labeled as chimera artifacts (red pathway). This provides reliable training labels. (c) ChimeraLM architecture. Input DNA sequences (batch size  $B$ , sequence length  $L$ ) are tokenized and encoded into hidden states  $\mathbf{H} \in \mathbb{R}^{L \times 256}$  through a backbone encoder (HyenaDNA [35]). Hyena operators capture long-range dependencies in genomic sequences. Attention pooling aggregates position-specific features using learned weights. Residual and multilayer perceptron (MLP) layers process pooled features, and a softmax layer outputs binary classification probabilities for biological versus artificial reads. (d) Attention pooling mechanism detail. The backbone encoder (HyenaDNA) transforms input sequences into hidden state  $\mathbf{H} \in \mathbb{R}^{L \times 256}$ . Attention weights  $\alpha \in \mathbb{R}^{L \times 1}$  are computed through linear layers, GELU activation, and softmax normalization, assigning importance scores to each nucleotide position. The weighted sum  $\mathbf{h}_{\text{pooled}} = \sum_{i=1}^L \alpha_i \mathbf{h}_i$  produces the pooled output  $\mathbf{h}_{\text{pooled}} \in \mathbb{R}^{256}$ , compressing variable-length sequences into fixed-dimensional representations. Created with BioRender.com.

sequencing (e.g., Oxford Nanopore Technologies (ONT)), base calling, and alignment to the reference genome. During amplification, template-switching events introduce artificial chimeric reads, resulting in alignment files that contain a mixture of authentic and artificial sequences. In downstream analysis, these artifacts can mimic SV and confound variant detection. To address this challenge, we developed ChimeraLM, a Genomic Language Model (GLM) designed to integrate directly into this analysis pipeline and distinguish biological reads from amplification-induced artifacts.	185
	186
	187
	188
	189
	190
	191
ChimeraLM functions as a pre-processing filter, operating after read alignment but before SV detection. It evaluates each chimeric read—sequences with multiple alignments to distant genomic locations—and classifies it as either biological (genuine) or artificial (WGA-induced). This binary decision enables the retention of authentic genomic sequences while removing amplification artifacts prior to variant calling. The resulting high-confidence biological reads are then passed to conventional SV detection algorithms for accurate identification of genomic rearrangements.	192
	193
	194
	195
	196
	197
	198
A high-confidence labeled dataset was required for supervised training of the model (Fig. 1b; Extended Data Fig. 1a). We constructed this dataset using sequencing data from the PC3 prostate cancer cell line, which provides both WGA-amplified and non-amplified (bulk) genomic data. The key assumption is that bulk sequencing contains only genuine genomic sequences, whereas WGA data includes both genuine and artificial chimeras. Chimeric reads from the PC3 WGA PromethION dataset were systematically compared against three independent bulk datasets (ONT PromethION, ONT MinION, and PacBio; see Methods). WGA reads whose chimeric structures were absent from all three bulk datasets were labeled artificial. Conversely, WGA reads with structures validated in one or more bulk datasets were labeled biological.	199
	200
	201
	202
	203
	204
	205
	206
	207
	208
Application of this labeling strategy to the PC3 WGA data (Extended Data Table 1) quantified the read distribution across these categories (Extended Data Fig. 1b). We identified 12,670,396 chimeric reads with zero matches in the bulk reference, which were classified as artificial. Conversely, we identified a total of 293,180 reads validated as biological. This biological set was composed of reads matching one (Match 1: 101,094 reads), two (Match 2: 190,309 reads), or all three (Match 3: 1,777 reads) of the bulk reference datasets. To construct a balanced training dataset, we retained all 293,180 biological reads (combining Match 1, 2, and 3) and subsampled an equal number (293,180) of artificial reads from the no-match category. This set was augmented with 178,748 chimeric reads subsampled from the bulk datasets as positive controls. The final dataset of 765,108 labeled reads was partitioned into training (70%), validation (20%), and internal test (10%) sets using stratified splitting.	209
	210
	211
	212
	213
	214
	215
	216
	217
	218
	219
	220
The architecture of ChimeraLM (Fig. 1c) was specifically designed to learn from this dataset by operating directly on raw DNA sequences, bypassing conventional, feature-based classifiers. This design must address three primary technical challenges: (1) efficiently processing variable-length sequences of many kilobases, (2) simultaneously maintaining single-nucleotide resolution to detect the precise, abrupt compositional changes that define chimeric junctions, and (3) aggregating variable-length sequence representations into a consistent classification output.	221
	222
	223
	224
	225
	226
	227
ChimeraLM first addresses the need for high resolution by tokenizing input sequences at the single-nucleotide level. This base-pair precision is required to preserve	228
	229
	230

231 the complete sequence information necessary for detecting chimeric junctions—the  
232 breakpoints where disparate genomic regions are artificially fused and which often  
233 exhibit abrupt compositional changes.

234 The architecture’s core employs Hyena operators [39], selected specifically to  
235 overcome the challenge of processing long DNA sequences. Traditional attention  
236 mechanisms scale quadratically with sequence length, making them computationally  
237 prohibitive for long-read data. Hyena operators, by contrast, achieve subquadratic  
238 scaling, enabling ChimeraLM to analyze full-length reads without fragmentation and  
239 thus preserve the structural context around chimeric junctions. To leverage existing  
240 genomic knowledge, we initialized the model with weights from HyenaDNA [35], a  
241 genomic foundation model pre-trained on diverse DNA sequences.

242 Finally, to produce a classification, the model employs an attention pooling mech-  
243 anism to aggregate information across the entire variable-length read (Fig. 1d). This  
244 module computes learned, position-specific weights to identify which nucleotides—such  
245 as those at the junction boundary—are most informative for the classification deci-  
246 sion. This weighted aggregation produces a fixed-dimensional representation, which  
247 is then processed through MLP components with residual connections. A final soft-  
248 max layer outputs the probability scores for the biological versus artificial classes (see  
249 Methods). This end-to-end architecture enables ChimeraLM to learn directly from  
250 raw sequence data, discovering complex patterns that may not be apparent through  
251 rule-based algorithms.

252

### 253 **ChimeraLM achieves high accuracy and reduces artifacts to 254 near-bulk levels across platforms**

255

256 We first evaluated ChimeraLM’s classification accuracy on the held-out test set  
257 (derived from the PromethION training data), which comprised reads with known bio-  
258 logical or artificial status (Fig. 2a). The model achieved an F1 score of 0.81, reflecting  
259 balanced sensitivity and specificity in artifact detection. A recall of 0.95 indicates that  
260 95% of true chimeric reads were correctly identified—critical for minimizing down-  
261 stream false-positive structural variant calls—while a precision of 0.70 shows that the  
262 majority of reads flagged as chimeric were true artifacts. These results establish the  
263 model’s reliability for identifying amplification-induced artifacts in long-read data.

264 We next assessed its practical effectiveness on the full PC3 WGA datasets, com-  
265 paring performance on the PromethION and MinION platforms (Fig. 2b). Bulk  
266 sequencing established a low baseline chimeric read rate (2.3% for PromethION; 2.5%  
267 for MinION). WGA dramatically increased this artifact load to 46.0% (PromethION)  
268 and 23.0% (MinION). After ChimeraLM filtering, chimeric content dropped to 4.9%  
269 on PromethION and 1.5% on MinION—representing 10- to 15-fold reductions—while  
270 retaining 15.8 million and 5.6 million biological reads. This restoration to near-bulk  
271 quality demonstrates that ChimeraLM effectively separates genuine genomic reads  
272 from WGA-induced artifacts.

273 We then benchmarked ChimeraLM against existing computational tools for  
274 detecting amplification-induced chimeras, SACRA [30] and 3rd-ChimeraMiner [23]  
275 (Fig. 2c,d). When applied to the same PromethION and MinION WGA data,  
276

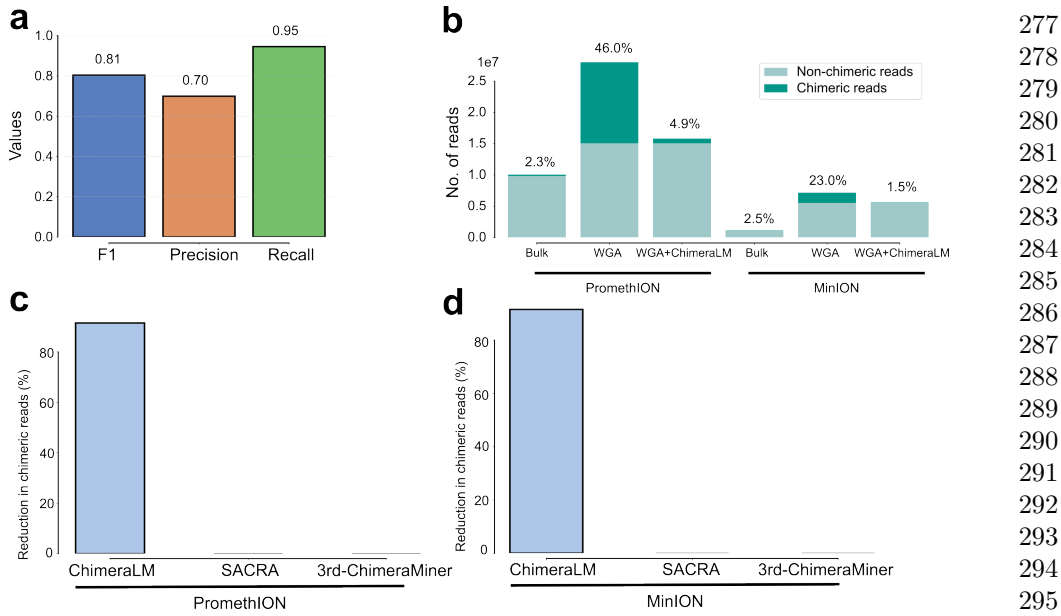


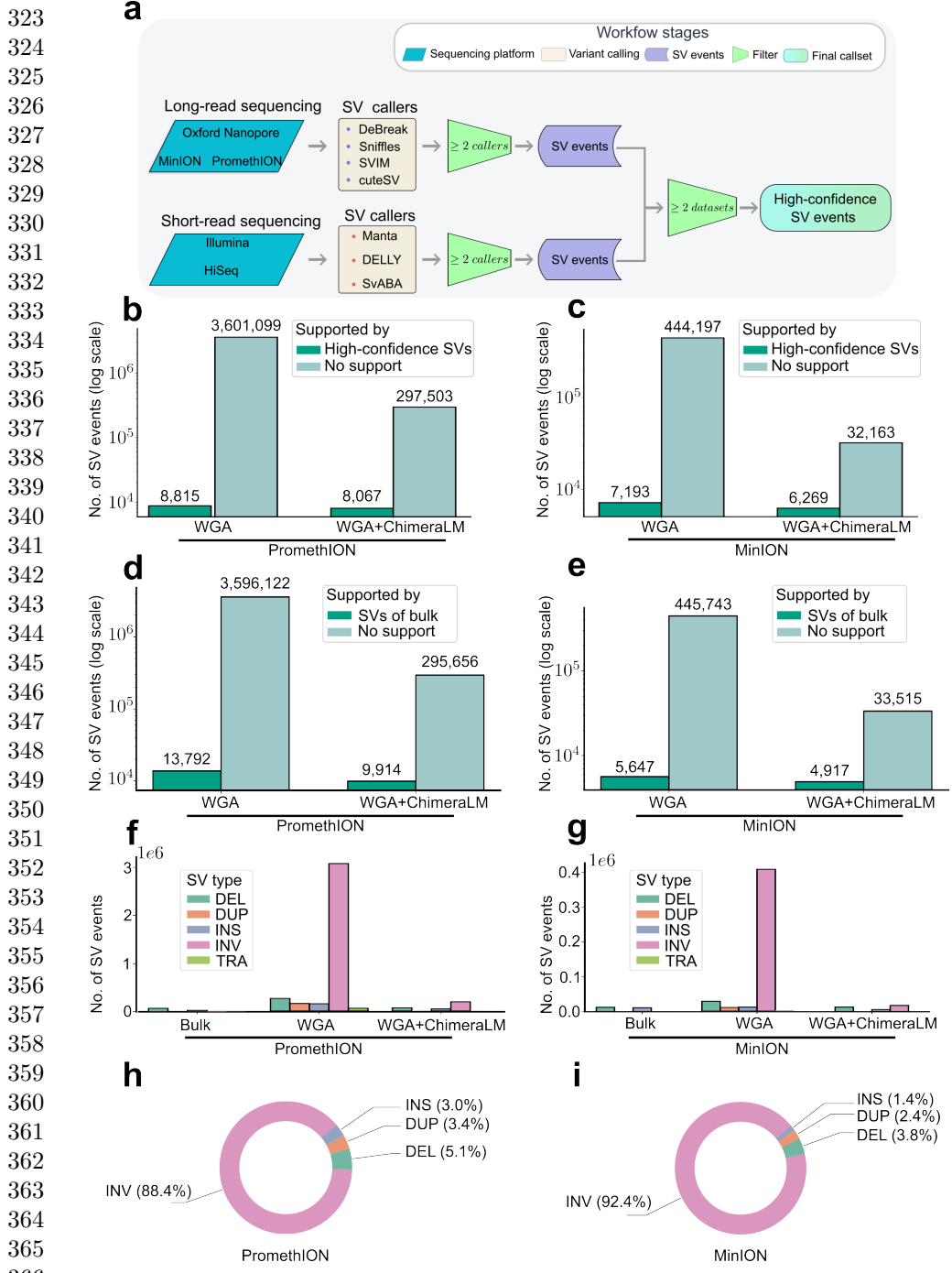
**Fig. 2 ChimeraLM accurately identifies and removes WGA-induced chimeric artifacts.**

(a) Classification performance on held-out test data. ChimeraLM achieves high recall (0.95) in identifying chimera artifacts while maintaining acceptable precision (0.70), yielding an F1 score of 0.81 for binary classification of biological versus artificial sequences. (b) Chimeric read reduction across sequencing platforms. Stacked bars show the proportion of chimeric (dark teal) and non-chimeric (light teal) reads in bulk sequencing, WGA-amplified samples, and ChimeraLM-filtered WGA samples. Data from PC3 cell line sequenced on PromethION (left) and MinION (right) platforms demonstrate that ChimeraLM reduces chimeric read frequencies from 46.0% to 4.9% (PromethION) and from 23.0% to 1.5% (MinION), approaching bulk levels (2.3% and 2.5%, respectively). (c,d) Benchmarking against existing methods. ChimeraLM achieves approximately 90% reduction in chimeric reads on both PromethION (c) and MinION (d) platforms, whereas existing computational tools SACRA and 3rd-ChimeraMiner show no detectable reduction in chimeric content.

ChimeraLM achieved an approximately 90% reduction in chimeric reads on both platforms. In stark contrast, neither SACRA nor 3rd-ChimeraMiner showed any detectable reduction in chimeric content (0% reduction).

Together, these results demonstrate robust and platform-agnostic performance. The strong filtering on the MinION dataset (Fig. 2b) is particularly noteworthy, as this platform served as a completely independent test set—the model was trained exclusively on PromethION data yet generalized effectively to MinION. This cross-platform generalization, combined with the high recall on the internal test set (Fig. 2a) and clear superiority over existing tools (Fig. 2c,d), confirms that ChimeraLM learns universal sequence-level features of WGA-induced artifacts rather than platform-specific technical signatures. This design principle—learning from DNA sequence patterns that are invariant across sequencing technologies—suggests ChimeraLM’s applicability extends beyond nanopore platforms to other long-read and short-read sequencing technologies.

277  
278  
279  
280  
281  
282  
283  
284  
285  
286  
287  
288  
289  
290  
291  
292  
293  
294  
295  
296  
297  
298  
299  
300  
301  
302  
303  
304  
305  
306  
307  
308  
309  
310  
311  
312  
313  
314  
315  
316  
317  
318  
319  
320  
321  
322



367 **Fig. 3 ChimeraLM improves structural variant detection accuracy.** (a) Construction of  
368 high-confidence SV reference dataset. PC3 bulk DNA was sequenced on multiple platforms (ONT  
PromethION and MinION, Illumina HiSeq) and analyzed with multiple SV calling algorithms. SV  
events detected by  $\geq 2$  callers on the same platform were retained. Events supported by both long-read  
and short-read platforms were designated as high-confidence gold standard SVs. (b,c) SV validation  
against multi-platform gold standard. Stacked bars show total SV calls (log scale, numbers above bars)  
classified as gold standard-supported (dark teal) or unsupported (light teal) for PromethION (b) and  
MinION (c). ChimeraLM substantially reduces unsupported SV calls while preserving gold standard  
events. (d,e) SV validation against long-read bulk sequencing (ONT PromethION and MinION).  
Stacked bars show SV calls classified as bulk-supported (dark teal) or unsupported (light teal) for  
PromethION (d) and MinION (e). Long-read bulk data from the same platform provides platform-  
matched validation, capturing true variants that may be specific to long-read detection. (f,g) SV type  
distribution across processing methods. Bar charts show the number of detected SVs by type: deletion  
(DEL) (green), duplication (DUP) (orange), insertion (INS) (blue), INV (pink), and translocation  
(TRA) (light green) for PromethION (f) and MinION (g). Unfiltered WGA data shows elevated counts  
across all types, particularly INVs and TRAs, which are reduced to bulk-like levels after ChimeraLM  
filtering. (h,i) Composition of chimeric artifact-supported SVs. Pie charts show the proportion of SV  
types among events supported exclusively by reads classified as chimeric artifacts in unfiltered WGA  
data for PromethION (h) and MinION (i). These represent false-positive SV calls that would be  
eliminated by ChimeraLM.

## ChimeraLM substantially reduces false-positive structural variant calls

Accurate **SV** detection is essential for understanding genomic diversity and disease mechanisms in single cells. However, **WGA**-induced chimeric artifacts can be misidentified as genuine **SVs**, leading to incorrect biological conclusions. To quantify ChimeraLM’s impact on **SV** calling accuracy, we compared variant calls from unfiltered **WGA** data and ChimeraLM-filtered data against two independent reference standards (Fig. 3).

We first established a high-confidence gold standard **SV** dataset by integrating results from bulk PC3 DNA sequenced on multiple platforms (**ONT** PromethION, **ONT** MinION, and Illumina HiSeq) and analyzed with multiple **SV** callers (Fig. 3a; Extended Data Table 1). **SVs** detected by  $\geq 2$  callers on the same platform and supported by both long-read and short-read data were retained as gold-standard events, ensuring high specificity across technologies.

Comparison against this gold standard revealed that unfiltered **WGA** data contained extensive false-positive **SVs** (Fig. 3b,c). On PromethION, raw **WGA** data produced 3.6 million **SV** calls, of which only 8,815 (0.24%) matched gold standard events—indicating that over 99% were artifacts. After ChimeraLM filtering, total calls dropped to 305,570 while retaining 8,067 true events, raising the validation rate to 2.64% (11-fold improvement) and preserving 91.5% of true variants. MinION data showed similar results, with calls reduced from 451,390 to 38,432 and the validation rate increasing from 1.59% to 16.3% (10-fold improvement) while retaining 87.2% of true variants. These results highlight ChimeraLM’s ability to remove spurious **SV** calls while maintaining biological sensitivity.

To complement this stringent validation, we next performed platform-matched bulk validation, comparing **WGA**-derived **SV** calls against long-read bulk sequencing from the same platform (Fig. 3d,e). This reference captures true **SVs** that may be missed by short-read data, providing a more inclusive measure of recall. Under this benchmark, ChimeraLM increased validation rates from 0.38% to 3.24% on PromethION (8.5-fold improvement) and from 1.25% to 12.79% on MinION (10-fold improvement), while retaining 71.9% and 87.1% of bulk-supported events, respectively. The consistent improvements across independent datasets demonstrate that ChimeraLM effectively suppresses **WGA**-induced artifacts without sacrificing detection of genuine **SVs**.

Together, these analyses demonstrate that ChimeraLM reduces false-positive **SV** calls by 8–11 fold while preserving 72–92% of true variants, resulting in a substantial enhancement of the signal-to-noise ratio in single-cell **SV** discovery. By restoring near-bulk specificity and maintaining robust sensitivity, ChimeraLM enables more accurate and interpretable downstream genomic analyses.

## ChimeraLM restores unbiased SV-type distributions and characterizes artifact composition

Amplification artifacts can distort the apparent spectrum of **SVs**, often inflating specific **SV** types. To evaluate whether ChimeraLM effectively corrects such distortions,

369  
370  
371  
372  
373  
374  
375  
376  
377  
378  
379  
380  
381  
382  
383  
384  
385  
386  
387  
388  
389  
390  
391  
392  
393  
394  
395  
396  
397  
398  
399  
400  
401  
402  
403  
404  
405  
406  
407  
408  
409  
410  
411  
412  
413  
414

415 we compared **SV** type distributions across bulk, unfiltered **WGA**, and ChimeraLM-  
416 filtered datasets (Fig. 3f,g). Bulk sequencing showed relatively balanced proportions  
417 of **DELs**, **DUPs**, **INSS**, **INVs**, and **TRAs**. In contrast, unfiltered **WGA** data exhibited  
418 a dramatic overrepresentation of **INVs** on both PromethION and MinION platforms,  
419 consistent with pervasive amplification artifacts. After ChimeraLM filtering, these dis-  
420 tributions were largely restored toward bulk-like profiles: excessive **INVs** were markedly  
421 reduced while other **SV** categories remained stable. This shift reflects selective removal  
422 of artifact-supported **INVs** rather than indiscriminate loss of genuine inversion signals,  
423 demonstrating high specificity in distinguishing chimeric from biological reads.

424 To investigate the basis of this normalization, we analyzed **SV** calls supported  
425 exclusively by reads classified as chimeric by ChimeraLM (Fig. 3h,i). These artifact-  
426 supported events were overwhelmingly dominated by **INVs**, comprising 88.4% on  
427 PromethION and 92.4% on MinION. This pattern is consistent with template-  
428 switching junctions that produce inversion-like alignment signatures. Smaller fractions  
429 of **DELs** (5.1% and 3.8%), **DUPs** (3.4% and 2.4%), and **INSS** (3.0% and 1.4%) were also  
430 observed, demonstrating that **WGA**-induced chimeras can mimic diverse **SV** categories  
431 rather than only **INVs**.

432 This characterization has important implications for single-cell genomics. Although  
433 **INVs** are the predominant artifact type, the coexistence of **DELs**, **DUPs**, and **INSS**  
434 among chimeric events indicates that comprehensive filtering—rather than inversion-  
435 specific correction—is essential for accurate **SV** detection. Without ChimeraLM  
436 filtering, single-cell **SV** analyses would be confounded not only by false-positive **INVs**  
437 but also by other artifact-associated variants [31, 32]. By restoring biologically repre-  
438 sentative **SV** type distributions, ChimeraLM enables robust and interpretable charac-  
439 terization of structural variation in single cells without distortion from **WGA**-induced  
440 artifacts.

441

442

443

444

445

446

447

448

449

450

451

452

453

454

455

456

457

458

459

460

461  
462  
463  
464  
465  
466  
467  
468  
469  
470  
471  
472  
473  
474  
475  
476  
477  
478  
479  
480  
481  
482  
483  
484  
485  
486  
487  
488  
489  
490  
491  
492  
493  
494  
495  
496  
497  
498  
499  
500  
501  
502  
503  
504  
505  
506

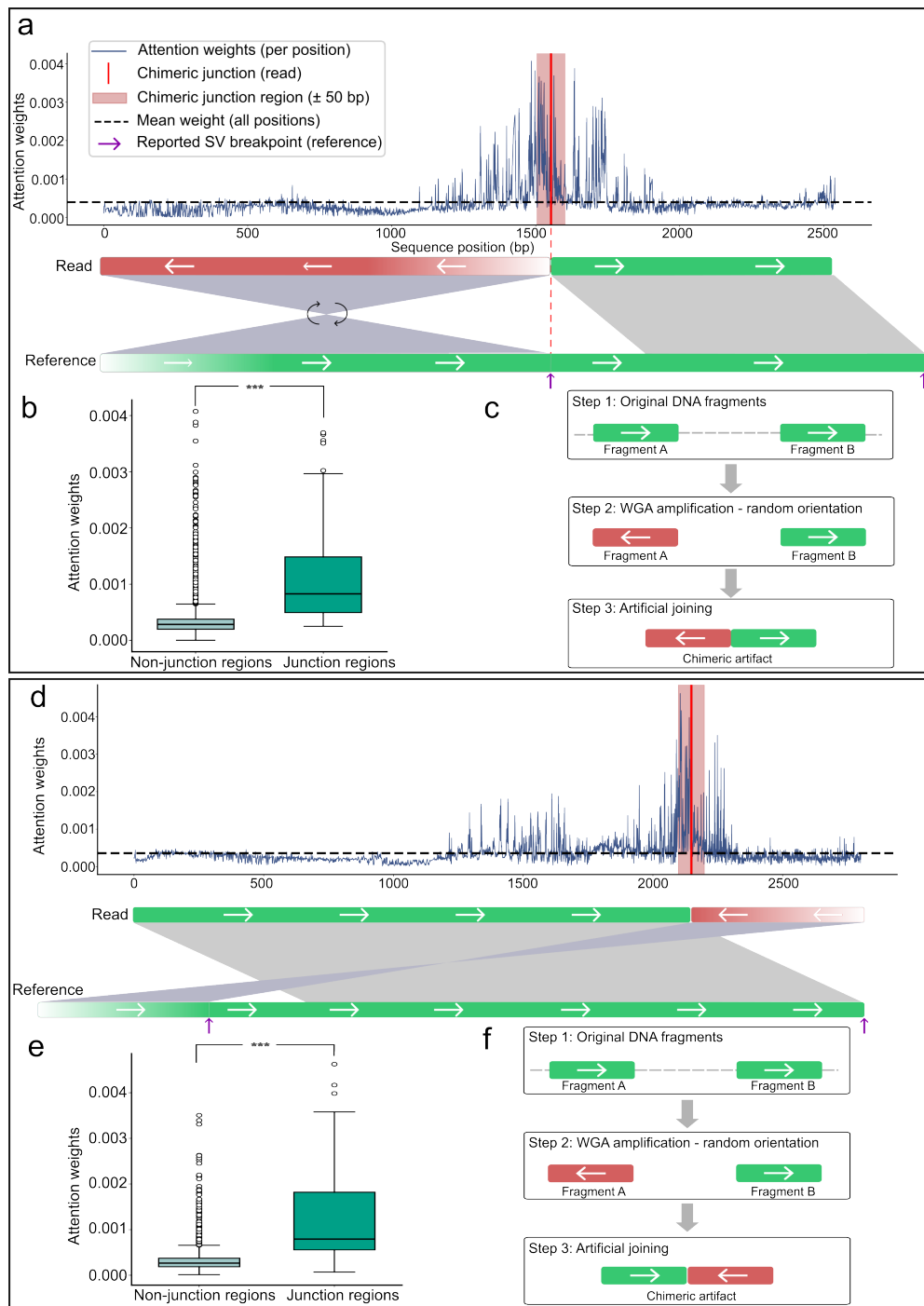


**Fig. 4 ChimeraLM attention weights can localize to chimeric junction regions.** (a,d) Attention weight profiles for two representative chimeric reads. Upper panels show attention weights per sequence position (blue line) and mean attention (dashed line). Red vertical lines mark chimeric junction positions, with pink shading indicating junction region ( $\pm 50$  bp). Purple arrows show reported SV breakpoints. Lower panels illustrate read alignments: reads (top bars) show orientation transitions at junctions (green = forward, red = reverse-complemented, arrows indicate strand), while reference genome (bottom bars) maintains continuous forward orientation. Gray regions connect aligned segments. (b,e) Quantitative attention analysis. Box plots show significantly elevated attention weights in junction region versus non-junction regions for both examples ( $p = 5.3 \times 10^{-14}$  and  $p = 6.8 \times 10^{-15}$ , respectively; Wilcoxon rank-sum test). (c,f) Proposed chimera formation mechanisms. Step 1: Original DNA fragments from distant genomic loci exist in forward orientation. Step 2: During WGA, one or both fragments may undergo random reverse-complementation. Step 3: Template switching joins the fragments with discordant orientations, creating chimeric artifacts. The two examples illustrate different orientation patterns (forward-to-reverse vs reverse-to-forward transitions) arising from random strand selection during amplification.

507 **ChimeraLM provides interpretable classification through  
508 attention visualization**

509 We next investigated whether ChimeraLM’s attention mechanism highlights biologi-  
510 cally meaningful regions within sequencing reads (Fig. 4).

512 For representative chimeric reads, attention weight profiles showed low baseline  
513 values across most positions but pronounced peaks at junction regions where tem-  
514 plate switching artificially joins DNA fragments from distinct genomic loci (Fig. 4a,d).  
515 These peaks coincided precisely with alignment breakpoints characterized by orienta-  
516 tion changes between adjacent read segments—the defining signature of **WGA**-induced  
517 chimeric artifacts.

518 Quantitative analysis confirmed that attention weights within junction regions  
519 ( $\pm 50$  bp) were significantly higher than those in non-junction regions (Wilcoxon rank-  
520 sum test,  $p = 5.3 \times 10^{-14}$  and  $p = 6.8 \times 10^{-15}$ ) (Fig. 4b,e). Such localization indicates  
521 that ChimeraLM learns mechanistically relevant features associated with artificial  
522 junction formation rather than relying on spurious correlations.

523 Schematic reconstruction of the amplification process further supports this inter-  
524 pretation (Fig. 4c,f). During **WGA**, DNA fragments from distant genomic loci may  
525 undergo random strand orientation changes before being joined by template switching.  
526 This process produces artificial junctions with discordant orientations—forward-to-  
527 reverse or reverse-to-forward—that generate inversion-like alignment signatures and  
528 are effectively recognized by the model’s attention peaks.

529 Together, these analyses demonstrate that ChimeraLM’s attention mechanism  
530 can localize chimeric junctions at single-base resolution and capture the underlying  
531 orientation discontinuities that define **WGA**-induced artifacts.

532 **533 Discussion**

534 **WGA** has enabled genomic analysis from single cells but introduces chimeric arti-  
535 facts that compromise **SV** detection. ChimeraLM addresses this challenge through  
536 sequence-level classification of biological versus artificial reads, substantially improving  
537 **SV** calling accuracy before downstream analysis. This upstream filtering strategy—  
538 removing problematic sequences at the read level rather than correcting errors post  
539 hoc—provides a practical solution for single-cell genomics laboratories.

540 Our results demonstrate several key advantages of ChimeraLM for long-read single-  
541 cell sequencing. The method achieves approximately 90% reduction in chimeric reads  
542 across nanopore platforms while retaining 72–92% of true **SVs**. It reduces false-positive  
543 **SV** calls by 8–11 fold, enabling researchers to focus on biologically relevant variants  
544 without manually filtering thousands of artifacts. Moreover, ChimeraLM performs  
545 consistently across PromethION and MinION without platform-specific retraining,  
546 indicating that it captures generalizable sequence features of **WGA**-induced chimeras.  
547 These results underscore the model’s robustness across diverse datasets and sequencing  
548 conditions.

549 ChimeraLM’s effectiveness reflects the ability of deep learning models to capture  
550 complex sequence patterns that are difficult to encode in rule-based filters. Tradi-  
551 tional quality control methods rely on predefined metrics such as mapping quality or

read depth [23, 30], which may not effectively distinguish chimeric artifacts from biological reads. By learning directly from sequence data, ChimeraLM discovers subtle compositional and structural features that differentiate authentic genomic sequences from amplification artifacts. Furthermore, the model offers interpretability through attention visualization, allowing researchers to examine which sequence regions drive classification. Attention weights can concentrate sharply at junctions where template switching joins DNA fragments from distinct loci, matching the known mechanism of chimera formation. Some reads show more diffuse attention distributions, suggesting that ChimeraLM integrates multiple complementary cues—such as junction orientation, compositional biases, and local sequence context—to classify diverse artifact types. This interpretability builds confidence in the model’s predictions and provides a lens for probing the molecular processes underlying amplification-induced artifacts.

The improved reliability of **SV** detection has direct implications for single-cell genomics. Studies of chromosomal instability, clonal evolution, and **SV** burden in individual cells have long been constrained by high false-positive rates in **WGA** data [31, 32]. ChimeraLM enables more confident identification of genuine **SVs**, supporting research in cancer genomics, developmental biology, and aging where single-cell resolution is essential for understanding cellular heterogeneity. Although the current model processes reads independently, integrating additional contextual features—such as coverage, mate-pair, or phasing information—could further enhance accuracy. **Graphics Processing Unit (GPU)** resources are recommended for large-scale datasets, while **Central Processing Unit (CPU)** inference remains feasible for smaller studies; runtime optimization and model compression may improve accessibility for broader use.

Future work should prioritize validation across diverse biological and technical contexts. First, testing on multiple cell types (primary, stem, or immune cells) and **WGA** protocols (**MALBAC**, **LIANTI**, **PTA**) will establish biological generalizability. Second, validation on additional sequencing platforms—including PacBio HiFi, Illumina linked-reads, and emerging long-read technologies—will confirm the platform-agnostic design principle. The sequence-level approach suggests ChimeraLM should transfer effectively to any platform, though platform-specific fine-tuning may optimize performance. Third, the interpretability of attention-based models could be leveraged to investigate mechanisms of chimera formation: large-scale analysis of attention patterns may reveal recurrent sequence motifs or genomic contexts associated with template switching, guiding the development of improved amplification protocols. More broadly, ChimeraLM illustrates the potential of **GLMs** for data quality control applications [35]. Architectural innovations such as the Hyena operator for efficient long-range modeling [39] may have utility beyond chimera detection, addressing challenges such as contamination, adapter artifacts, and systematic sequencing errors across multiple platforms.

Looking ahead, ChimeraLM’s framework could extend beyond single-cell genomics to address quality control challenges in other amplification-dependent technologies, including cell-free DNA analysis, ancient DNA studies, and metagenomic sequencing from low-biomass samples. The model’s interpretability through attention visualization also opens opportunities for mechanistic studies of polymerase fidelity and

599 template-switching dynamics across different amplification protocols. Furthermore,  
600 integration with emerging single-cell multi-omics platforms could enable simultaneous  
601 quality control across genomic, transcriptomic, and epigenomic data layers, providing  
602 a unified framework for artifact detection in complex single-cell experiments.

603 ChimeraLM thus provides a practical and interpretable framework for improving  
604 long-read single-cell genomic data quality. By removing WGA-induced chimeric arti-  
605 facts at the read level and revealing the mechanistic features that drive them, the  
606 method not only enhances SV detection reliability but also deepens understanding of  
607 amplification-induced bias in single-cell genomics.

608

## 609 **Methods**

610

### 611 **Cell culture, single-clone preparation, and nanopore sequencing**

#### 612 *Cell culture and single-clone establishment*

613 PC3 prostate cancer cells (ATCC® CRL-1435™) were cultured in RPMI-1640 medium  
614 supplemented with 10% fetal bovine serum and 1% penicillin-streptomycin at 37 °C  
615 with 5% CO<sub>2</sub>. To minimize biological heterogeneity, a monoclonal population was  
616 established by serial dilution in 96-well plates, ensuring that each culture originated  
617 from a single cell. Mycoplasma contamination was routinely tested and confirmed  
618 negative prior to DNA extraction.

619

#### 620 *DNA extraction and whole-genome amplification*

621 From the monoclonal population, two types of DNA samples were prepared: a  
622 bulk (non-amplified) control and ten single-cell MDA-amplified genomes. Bulk high-  
623 molecular-weight DNA was extracted using the Monarch® HMW DNA Extraction  
624 Kit for Cells & Blood (New England Biolabs). Individual cells were isolated using  
625 1CellDish-60 mm (iBiochips) and amplified using the REPLI-g Advanced DNA Sin-  
626 gle Cell Kit (Qiagen) following the manufacturer's protocol. DNA concentration and  
627 fragment integrity were assessed with a Qubit 4 fluorometer and Agilent TapeStation  
628 (DNA 1000/5000 ScreenTape). Only samples meeting quality standards were used for  
629 library construction.

630

#### 631 *Nanopore library preparation and sequencing*

632 Sequencing libraries were prepared using the ONT Ligation Sequencing Kit V14 (SQK-  
633 LSK114) and sequenced on MinION Mk1C or PromethION P2 Solo devices with  
634 R10.4.1 flow cells according to the manufacturer's genomic DNA workflow. Because  
635 all single-cell samples originated from the same monoclonal lineage, observed differ-  
636 ences between amplified and bulk data primarily reflect MDA-induced artifacts rather  
637 than biological variation, providing a controlled experimental setting for downstream  
638 analyses.

639

#### 640 *Basecalling and read processing*

641 Raw signal files (POD5) were basecalled using Dorado v0.5.0 with the high-accuracy  
642 model dna\_r10.4.1\_e8.2\_400bps\_hac@v4.3.0 [40]. Reads with mean quality < 10

or length < 500 bp were removed. Residual adapters and concatemers were trimmed using Cutadapt v4.0 [41] in two-pass error-tolerant mode. Cleaned reads were aligned to the GRCh38.p13 reference genome using minimap2 v2.26 (`map-ont` preset) [42]. Resulting BAM files were sorted and indexed with SAMtools v1.16 [43]. Read length and mapping statistics were calculated using NanoPlot v1.46.1 [44]. All samples were processed under identical parameters to ensure consistency across datasets.

### ***Chimeric read identification***

Chimeric reads were identified based on the presence of supplementary alignments in BAM files using the **Supplementary Alignment (SA)** tag. The **SA** tag indicates that a read has additional alignments beyond the primary alignment, which is characteristic of chimeric sequences that map to multiple distant genomic locations. To ensure accurate identification, we applied stringent filtering criteria: reads were classified as chimeric only if they (1) were not unmapped, (2) contained the **SA** tag, (3) were not secondary alignments, and (4) were not supplementary alignments themselves. This filtering approach ensures that only primary alignments with supplementary mapping evidence are considered chimeric, avoiding double-counting of the same chimeric event and excluding low-quality or ambiguous alignments. Reads without the **SA** tag (single continuous alignments) were classified as non-chimeric. This approach leverages the standard BAM format specification to reliably identify reads with complex alignment patterns.

## **Training data construction**

### ***Data generation and sources***

To construct the training dataset, we generated **WGA** and bulk sequencing data from PC3 cells. The **WGA** sample was amplified and sequenced on the PromethION P2 platform (**ONT**), while three independent bulk datasets were produced from non-amplified genomic DNA: bulk PromethION P2, bulk MinION Mk1c (**ONT**), and bulk PacBio. These bulk datasets represent authentic biological sequences free from amplification-induced artifacts. In contrast, **WGA** sequencing includes both genuine genomic reads and artificial chimeras introduced during the amplification process. An additional **WGA** dataset sequenced on the MinION Mk1c platform was reserved exclusively as an independent test set for cross-platform evaluation.

### ***Ground truth annotation and class definition***

Ground truth labels were established by systematically comparing chimeric reads from the **WGA** PromethION P2 dataset against those from the three bulk datasets. For each **WGA** chimeric read, all alignment segments—defined by their genomic start and end coordinates—were compared to the corresponding segments of bulk chimeric reads. A **WGA** read was labeled as biological if every segment matched at least one bulk chimeric read within a 1 kb positional tolerance, indicating that the structural configuration is also present in non-amplified DNA. Reads lacking any matching pattern across all bulk datasets were labeled as artificial chimeras, presumed to arise from the amplification process. To ensure balanced class representation, additional

691 chimeric reads were randomly sampled from the bulk datasets and labeled as biological,  
692 as these reads originate from genuine genomic rearrangements such as true **SVs**.  
693 The final labeled dataset combined the annotated **WGA** PromethION P2 reads with  
694 the subsampled bulk chimeric reads and was subsequently partitioned into training,  
695 validation, and test sets as described below.

696

#### 697 *Dataset partitioning and cross-platform validation*

698 The combined labeled dataset, derived from **WGA** PromethION P2 and bulk sequencing  
699 data, was divided into training (70%), validation (20%), and internal test (10%)  
700 sets using stratified random sampling to maintain class balance. These subsets  
701 were used respectively for model training, hyperparameter tuning, and performance  
702 evaluation on data from the same sequencing platform.

703 To evaluate cross-platform generalization, the complete **WGA** MinION Mk1c  
704 dataset was reserved as an independent external test set. This dataset, generated on a  
705 different nanopore platform, was never used during model training or internal testing.  
706 This two-level evaluation design allowed us to test whether ChimeraLM captures general  
707 sequence features of amplification-induced chimeras rather than platform-specific  
708 artifacts.

709

## 710 Model architecture

711

### 712 *Backbone encoder*

713 ChimeraLM employs the pre-trained HyenaDNA model [35] as its backbone encoder.  
714 This model was pre-trained on large-scale genomic data and provides robust sequence  
715 representations. DNA sequences are tokenized at single-nucleotide resolution, with  
716 each base (A, C, G, T, N) mapped to a unique integer token (7, 8, 9, 10, 11, respectively).  
717 Special tokens include [CLS]=0, [PAD]=4, and others for sequence processing.  
718 Input sequences are truncated at 32,768 bp or padded to enable batch processing.

719 For a tokenized input sequence  $\mathbf{x} \in \mathbb{Z}^L$ , the HyenaDNA backbone generates  
720 contextualized hidden representations:

721

$$722 \quad \mathbf{H} = \text{HyenaDNA}(\mathbf{x}) \in \mathbb{R}^{L \times 256}$$

723

724 where  $\mathbf{H} = (\mathbf{h}_1, \mathbf{h}_2, \dots, \mathbf{h}_L)$  represents position-wise hidden states with dimension 256.  
725 The Hyena operators [39] efficiently capture both local sequence motifs and long-range  
726 dependencies essential for distinguishing biological sequences from chimeric artifacts.

727

### 728 *Attention pooling*

729 To aggregate variable-length sequence representations into fixed-size vectors,  
730 ChimeraLM implements attention-based pooling. For hidden states  $\mathbf{H} \in \mathbb{R}^{L \times 256}$ ,  
731 attention weights are computed through a two-layer network:

732

$$733 \quad \mathbf{e} = \text{GELU}(\text{Linear}_{256 \rightarrow 256}(\mathbf{H})) \in \mathbb{R}^{L \times 256}$$

734

$$735 \quad \mathbf{s} = \text{Linear}_{256 \rightarrow 1}(\mathbf{e}) \in \mathbb{R}^{L \times 1}$$

736

$$\alpha = \text{softmax}(\mathbf{s}) \in \mathbb{R}^{L \times 1}$$

The pooled representation is the weighted sum of hidden states:	737
	738
$\mathbf{h}_{\text{pooled}} = \sum_{i=1}^L \alpha_i \mathbf{h}_i \in \mathbb{R}^{256}$	739
	740
	741
This mechanism assigns learned importance weights to each sequence position, enabling the model to focus on informative regions while accommodating natural variability in read lengths.	742
	743
	744
	745
<b>Classification head</b>	746
The pooled representation is processed through a <b>MLP</b> with residual connections. The first layer expands dimensionality:	747
	748
	749
$\mathbf{f}_1 = \text{Dropout}_{0.1}(\text{GELU}(\text{Linear}_{256 \rightarrow 512}(\mathbf{h}_{\text{pooled}}))) \in \mathbb{R}^{512}$	750
Subsequent residual blocks with input $\mathbf{f}_{\text{in}} \in \mathbb{R}^{512}$ compute:	751
	752
$\mathbf{f}_{\text{out}} = \text{Dropout}_{0.1}(\text{Linear}_{512 \rightarrow 512}(\text{GELU}(\text{Linear}_{512 \rightarrow 512}(\mathbf{f}_{\text{in}})))) + \mathbf{f}_{\text{in}}$	753
where the skip connection enables stable gradient flow during training. The final layer produces binary classification logits:	754
	755
	756
	757
	758
	759
$\mathbf{z} = [z_0, z_1] = \text{Linear}_{512 \rightarrow 2}(\mathbf{f}_{\text{final}}) \in \mathbb{R}^2$	760
where $z_0$ and $z_1$ represent logits for biological and artificial chimeric classes, respectively. During inference, the predicted class is $\hat{y} = \text{argmax}_{i \in \{0,1\}} z_i$ .	761
	762
	763
<b>Model summary</b>	764
The complete ChimeraLM pipeline processes DNA sequences through: (1) single-nucleotide tokenization, (2) HyenaDNA backbone encoding to generate contextualized representations, (3) attention pooling to aggregate position-specific features, (4) <b>MLP</b> layers with residual connections to learn classification features, and (5) binary classification output. The entire model is trained end-to-end using labeled <b>WGA</b> and bulk sequencing data.	765
	766
	767
	768
	769
	770
	771
	772
<b>Model training and optimization</b>	773
<b>Training configuration</b>	774
ChimeraLM was trained using PyTorch [45] and PyTorch Lightning [46] frameworks. Input sequences were tokenized using the tokenizer with maximum sequence length of 32,768 bp. Sequences longer than this threshold were truncated; shorter sequences were padded to enable batch processing. Training employed mixed-precision computation (bf16) to accelerate training while maintaining numerical stability.	775
	776
	777
	778
	779
	780
	781
	782

783 ***Optimization procedure***

784 We used the AdamW optimizer [47] with learning rate  $\eta = 1 \times 10^{-4}$  and weight  
 785 decay  $\lambda = 0.01$ . AdamW implements adaptive learning rates with decoupled weight  
 786 decay, combining the benefits of Adam optimization with proper L2 regularization.  
 787 A ReduceLROnPlateau scheduler dynamically adjusted the learning rate based on  
 788 validation loss, reducing it by a factor of 0.1 when no improvement occurred for 10  
 789 consecutive epochs. Early stopping with patience of 10 epochs prevented overfitting  
 790 by terminating training when validation performance plateaued. A fixed random seed  
 791 (12345) ensured reproducibility across training runs.

792 The training objective used cross-entropy loss for binary classification. For a train-  
 793 ing example with true class label  $y \in \{0, 1\}$  and model logits  $\mathbf{z} = [z_0, z_1]$ , the loss  
 794 is:

$$795 \quad \mathcal{L}(\mathbf{z}, y) = -\log \left( \frac{\exp(z_y)}{\exp(z_0) + \exp(z_1)} \right) = -z_y + \log(\exp(z_0) + \exp(z_1))$$

797 where  $z_0$  and  $z_1$  represent logits for biological and artificial chimeric classes, respec-  
 798 tively.

799

800 ***Training implementation***

801 Training used batch size of 16 sequences with 30 parallel data loading workers. GPU  
 802 acceleration was employed for efficient processing, with training typically requiring 96-  
 803 120 hours depending on dataset size. Model checkpointing saved the best-performing  
 804 model based on validation metrics. Configuration management used Hydra [48] to  
 805 enable reproducible experimentation.

806

807 ***Model evaluation***

808

809 Performance was monitored using accuracy, precision, recall, and F1 score on the  
 810 validation set after each epoch:

$$811 \quad \text{Precision} = \frac{\text{TP}}{\text{TP} + \text{FP}}, \quad \text{Recall} = \frac{\text{TP}}{\text{TP} + \text{FN}}$$

$$814 \quad \text{F1} = \frac{2 \times \text{Precision} \times \text{Recall}}{\text{Precision} + \text{Recall}}, \quad \text{Accuracy} = \frac{\text{TP} + \text{TN}}{\text{TP} + \text{TN} + \text{FP} + \text{FN}}$$

815

816 where TP (true positives) are chimeric reads correctly classified as artificial, TN (true  
 817 negatives) are biological reads correctly classified as biological, FP (false positives)  
 818 are biological reads misclassified as artificial, and FN (false negatives) are chimeric  
 819 reads misclassified as biological. Final model selection was based on best validation  
 820 performance as determined by early stopping.

821

822 ***Model inference and application***

823

824 ***Inference pipeline***

825

826 To apply ChimeraLM to new WGA sequencing data, the model takes a BAM file as  
 827 input. Chimeric reads are identified using SA tags and filtered to exclude unmapped,  
 828 secondary, or supplementary alignments. Each chimeric read sequence is tokenized

using the tokenizer (maximum length 32,768 bp, with truncation or padding as needed). The trained model processes sequences in batches, generating two logits  $[z_0, z_1]$  for each read corresponding to biological and artificial chimeric classes. Classification is determined by  $\hat{y} = \text{argmax}(z_0, z_1)$ . ChimeraLM outputs a filtered BAM file containing only reads classified as biological, which can be directly used for downstream analyses including **SV** calling.

## Performance evaluation

### *Test set evaluation*

Final model performance was evaluated on the held-out test set and the independent MinION Mk1c dataset. Metrics (precision, recall, F1 score, accuracy) were computed as described in the training section, where true positives represent chimeric reads correctly classified as artificial and true negatives represent biological reads correctly classified as biological.

### *SV calling*

**SVs** were called using multiple tools to ensure comprehensive detection. For long-read data (ONT PromethION P2 and MinION Mk1c), we used Sniffles v2.5 [24, 25], DeBreak v1.2 [26], SVIM v2.0.0 [27], and cuteSV v2.1.1 [28]. For short-read data of the PC3 cell line, we used both the CCLE Illumina whole-genome sequencing dataset and the PRJNA361315 Illumina WGS dataset, processed with Manta v1.6.0 [49], DELLY v1.5.0 [50], and SvABA v1.1.0 [51]. All tools were executed with default recommended parameters.

### *Gold standard SV dataset construction*

A high-confidence gold standard **SV** dataset was generated from bulk PC3 sequencing data to evaluate the impact of ChimeraLM on **SV** detection accuracy (Fig. 3a). All **SV** comparison and breakpoint correction were performed using OctopusSV v0.2.3 [52]. We used four datasets: bulk MinION Mk1c, bulk PromethION P2, the CCLE Illumina WGS dataset, and the PRJNA361315 Illumina WGS dataset. Within each dataset, **SV** events supported by at least two independent callers were retained. Variants supported by two or more datasets were designated as gold standard **SVs** for benchmarking.

### *SV benchmarking analysis*

To assess the impact of ChimeraLM on **SV** calling accuracy, we compared **SV** calls from unfiltered **WGA** data and ChimeraLM-filtered **WGA** data against two references: (1) the stringent multi-platform gold standard dataset, and (2) platform-matched long-read bulk sequencing data. Benchmarking was performed using Truvari v4.2.2 [53] with default parameters. **SVs** were considered supported if they matched reference variants within the defined breakpoint tolerance. Validation rates were calculated as the proportion of called **SVs** supported by the reference. This dual benchmarking strategy quantifies both improvements in detecting high-confidence multi-platform **SVs** and the retention of platform-specific true variants.

875 **Benchmarking against existing methods**

876 ChimeraLM was compared to two existing computational methods for detecting  
877 amplification-induced chimeric artifacts: SACRA [30] (GitHub commit 9a2607e) and  
878 3rd-ChimeraMiner [23] (GitHub commit 04b5233). Both tools were applied to **WGA**  
879 data from PromethION P2 and MinION Mk1c platforms using default parameters as  
880 recommended in their documentation. Performance was evaluated by measuring the  
881 percentage reduction in chimeric reads relative to unprocessed **WGA** data. Chimeric  
882 reads were identified using **WGA** tag-based alignment criteria (reads with **SA** tags  
883 indicating split alignments), and reduction rates were calculated as the proportion of  
884 chimeric reads removed by each method.  
885

886 **Attention weight analysis**  
887

888 To investigate ChimeraLM’s interpretability, we analyzed attention weights from  
889 the pooling mechanism for representative chimeric reads. Attention weights indicate  
890 the relative importance assigned to each sequence position during classification. For  
891 selected reads, we extracted per-position attention weights and visualized them along-  
892 side read alignments to identify whether the model focuses on mechanistically relevant  
893 regions.

894 Chimeric junction positions were identified from alignment data (defined by break-  
895 points in **SA** tags). A window of  $\pm 50$  bp surrounding each junction was designated as  
896 the junction region. Attention weights within junction region were compared to non-  
897 junction regions using the Wilcoxon rank-sum test [54], with statistical significance  
898 assessed at  $p < 0.001$ .  
899

900 **Data visualization**

901 Figures were generated using Python with Matplotlib [55] and Seaborn [56].

902 **Computing resources**

903 Computations were performed on a **High Performance Computing (HPC)** server with  
904 64-core Intel Xeon Gold 6338 CPU, 256 GB RAM, and two NVIDIA A100 **GPUs** (80  
905 GB memory each).

906 **Supplementary information.**

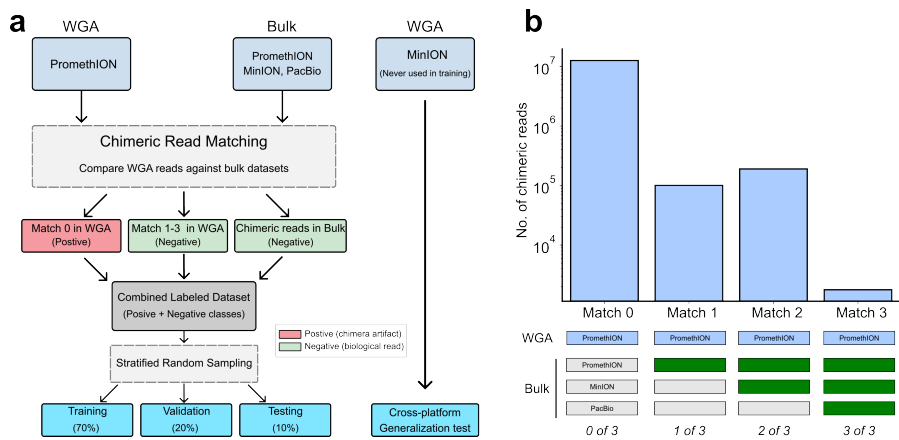
907 **Acknowledgements.** We thank Tingyou Wang for guidance on figure preparation.  
908 This project was supported in part by NIH grants R35GM142441 and R01CA259388  
909 awarded to RY.  
910

911 **Declarations**

912 **Author Contributions.** YL, QG and RY designed the study. YL and QG per-  
913 formed the analysis. QG performed the experiments. YL and QG designed and  
914 implemented the model. YL built the command-line tool and documentation. YL, QG  
915 and RY wrote the manuscript. RY supervised this work.  
916

**Extended Data Table 1** Sequencing and alignment statistics of PC3

Sample	Platform	Reads ( $\times 10^6$ )	Total bases (Gb)	Total bases aligned (Gb)	Fraction aligned	Mean length (bp)	Mean quality (Q)	Average identity (%)
WGA	MinION	9.11	14.6	10.4	0.7	1,603	14.3	97.6
WGA	PromethION	44.69	128.2	69.2	0.5	2,869	14.5	96.1
Bulk	MinION	0.97	8.1	7.1	0.9	8,310	17.2	97.3
Bulk	PromethION	8.00	69.9	62.4	0.9	8,732	18.5	97.7



**Extended Data Fig. 1 Training dataset construction and ground-truth labeling strategy for PC3 cell line.** (a) Schematic workflow for generating labeled training data. **WGA** PromethION data containing both biological and artificial chimeric reads is compared against three independent bulk sequencing datasets from the same cell line (PromethION, MinION, and PacBio platforms). Chimeric reads are classified through systematic matching: reads with no matches across all bulk datasets (Match 0) are labeled as artificial chimeras (positive class, red); reads matching one or more bulk datasets (Match 1–3) are labeled as biological reads (negative class, green), along with chimeric reads sampled directly from bulk data. The combined labeled dataset undergoes stratified random sampling to generate training (70%), validation (20%), and testing (10%) sets for model development. The **WGA** MinION dataset is reserved as an independent cross-platform generalization test set. (b) Distribution of chimeric read matches between **WGA** and bulk sequencing datasets. Bar chart showing the number of chimeric reads (y-axis, log scale) grouped by how many bulk datasets (x-axis) contained matching chimeric structures when comparing **WGA** PromethION reads against bulk sequencing data. “Match 0” indicates reads with no matches in any bulk dataset (classified as artificial chimeras,  $\sim 10^7$  reads), whereas “Match 1–3” indicate reads with matches in one, two, or all three bulk datasets (classified as biological reads,  $\sim 10^5$  reads each). Color-coded boxes below bars indicate which bulk platforms validated each read category: PromethION (light blue), MinION (white), and PacBio (white); green boxes indicate platform-specific validation. The substantial imbalance between Match 0 ( $\sim 10^7$ ) and Match 1–3 categories ( $\sim 10^5$  each) reflects the high prevalence of **WGA**-induced artifacts, necessitating balanced subsampling for supervised learning.

**Data Availability.** The raw sequencing data generated in this study have been deposited in the NCBI Sequence Read Archive (SRA) under BioProject accession

967 PRJNA1354861. The dataset includes Oxford Nanopore long-read whole-genome  
968 sequencing of PC3 prostate cancer cells and MDA-amplified single-cell derivatives. The  
969 individual SRA accessions are as follows: PC3 bulk (MinION Mk1C), SRR35904028;  
970 PC3 bulk (PromethION P2), SRR35904029; PC3 10-cell WGA (MinION Mk1C),  
971 SRR35904026; PC3 10-cell WGA (PromethION P2), SRR35904027. We can access the  
972 data at the following link: <https://dataview.ncbi.nlm.nih.gov/object/PRJNA1354861?reviewer=viej6cv6mgbli3n7a9a5k1bsb3>  
973

974 **Code Availability.** ChimeraLM, implemented in Python, is open source and  
975 available on GitHub (<https://github.com/ylab-hi/ChimeraLM>) under the Apache  
976 License, Version 2.0. The package can be installed via PyPI (<https://pypi.org/project/chimeralm>) using pip, with wheel distributions provided for Windows, Linux, and  
977 macOS to ensure easy cross-platform installation. An interactive demo is available on  
978 Hugging Face (<https://huggingface.co/spaces/yangliz5/ChimeraLM>), allowing users  
979 to test DeepChopper's functionality without local installation. For large-scale anal-  
980 yses, we recommend using ChimeraLM on systems with **GPU** acceleration. Detailed  
981 system requirements and optimization guidelines are available in the repository's  
982 documentation (<https://ylab-hi.github.io/ChimeraLM/>).  
983

984 **Conflict of interest.** RY has served as an advisor/consultant for Tempus AI, Inc.  
985 This relationship is unrelated to and did not influence the research presented in this  
986 study.  
987

988

## 989 **Acronyms**

990

991 **CPU** Central Processing Unit [13](#)

992

993 **DEL** deletion [8, 10](#)

994 **dMDA** droplet-based MDA [2](#)

995 **DOP-PCR** Degenerate Oligonucleotide-Primed PCR [2](#)

996 **DUP** duplication [8, 10](#)

997

998 **GLM** Genomic Language Model [5, 13](#)

999 **GPU** Graphics Processing Unit [13, 18, 20, 22](#)

1000

1001 **HPC** High Performance Computing [20](#)

1002

1003 **INS** insertion [8, 10](#)

1004 **INV** inversion [1, 8, 10](#)

1005 **LIANTI** Linear Amplification via Transposon Insertion [2, 13](#)

1006

1007 **MALBAC** Multiple Annealing and Looping-based Amplification Cycles [2, 13](#)

1008 **MDA** Multiple Displacement Amplification [2](#)

1009 **MLP** multilayer perceptron [4, 6, 17](#)

1010

1011 **ONT** Oxford Nanopore Technologies [5, 8, 9, 14, 15](#)

1012

<b>PTA</b> Primary Template-directed Amplification <a href="#">2</a> , <a href="#">13</a>	1013
<b>SA</b> Supplementary Alignment <a href="#">15</a> , <a href="#">18</a> , <a href="#">20</a>	1014
<b>SV</b> Structural Variation <a href="#">1–5</a> , <a href="#">8–14</a> , <a href="#">16</a> , <a href="#">19</a>	1015
<b>TRA</b> translocation <a href="#">8</a> , <a href="#">10</a>	1016
<b>WGA</b> Whole Genome Amplification <a href="#">1–21</a>	1017
 <b>References</b>	
[1] Kalef-Ezra, E. <i>et al.</i> Single-cell somatic copy number variants in brain using different amplification methods and reference genomes. <i>Communications Biology</i> 1288 (2024).	1018
[2] Sun, C. <i>et al.</i> Mapping recurrent mosaic copy number variation in human neurons. <i>Nature Communications</i> 4220 (2024).	1019
[3] Navin, N. <i>et al.</i> Tumour evolution inferred by single-cell sequencing. <i>Nature</i> <b>472</b> , 90–94 (2011).	1020
[4] Macaulay, I. C. & Voet, T. Single cell genomics: Advances and future perspectives. <i>PLOS Genetics</i> <b>10</b> , e1004126 (2014).	1021
[5] Leung, M. L. <i>et al.</i> Highly multiplexed targeted dna sequencing from single nuclei. <i>Nature Protocols</i> 214–235 (2016).	1022
[6] Gawad, C., Koh, W. & Quake, S. R. Single-cell genome sequencing: current state of the science. <i>Nature Reviews Genetics</i> 175–188 (2016).	1023
[7] Chen, C. <i>et al.</i> Single-cell whole-genome analyses by linear amplification via transposon insertion (LIANTI). <i>Science (new York, N.Y.)</i> <b>356</b> , 189–194 (2017).	1024
[8] Zong, C., Lu, S., Chapman, A. R. & Xie, X. S. Genome-wide detection of single-nucleotide and copy-number variations of a single human cell. <i>Science</i> 1622–1626 (2012).	1025
[9] Huang, L., Ma, F., Chapman, A., Lu, S. & Xie, X. S. Single-cell whole-genome amplification and sequencing: methodology and applications. <i>Annual Review of Genomics and Human Genetics</i> 79–102 (2015).	1026
[10] Dean, F. B. <i>et al.</i> Comprehensive human genome amplification using multiple displacement amplification. <i>Proceedings of the National Academy of Sciences</i> <b>99</b> , 5261–5266 (2002).	1027
[11] Lasken, R. S. & Stockwell, T. B. Mechanism of chimera formation during the multiple displacement amplification reaction. <i>BMC Biotechnology</i> <b>7</b> , 19 (2007).	1028

- 1059 [12] Pinard, R. *et al.* Assessment of whole genome amplification-induced bias through  
1060 high-throughput, massively parallel whole genome sequencing. *BMC Genomics*  
1061 **7**, 216 (2006).
- 1062
- 1063 [13] Telenius, H. *et al.* Degenerate oligonucleotide-primed PCR: General amplification  
1064 of target DNA by a single degenerate primer. *Genomics* **13**, 718–725 (1992).
- 1065
- 1066 [14] Gonzalez-Pena, V. *et al.* Accurate genomic variant detection in single cells with  
1067 primary template-directed amplification. *Proceedings of the National Academy of  
1068 Sciences* **118**, e2024176118 (2021).
- 1069
- 1070 [15] Hård, J. *et al.* Long-read whole-genome analysis of human single cells. *Nature  
1071 Communications* **14**, 5164 (2023).
- 1072
- 1073 [16] Dippenaar, A. *et al.* Droplet based whole genome amplification for sequencing  
1074 minute amounts of purified mycobacterium tuberculosis DNA. *Scientific Reports*  
1075 **14**, 9931 (2024).
- 1076
- 1077 [17] de Bourcy, C. F. A. *et al.* A quantitative comparison of single-cell whole genome  
1078 amplification methods. *PLoS ONE* e105585 (2014).
- 1079
- 1080 [18] Biezuner, T. *et al.* Comparison of seven single cell whole genome amplification  
1081 commercial kits using targeted sequencing. *Scientific Reports* 17171 (2021).
- 1082
- 1083 [19] Fu, Y. *et al.* Uniform and accurate single-cell sequencing based on emulsion  
1084 whole-genome amplification. *Proceedings of the National Academy of Sciences*  
1085 11923–11928 (2015).
- 1086
- 1087 [20] Agyabeng-Dadzie, F. *et al.* Evaluating the benefits and limits of multiple displace-  
1088 ment amplification with whole-genome oxford nanopore sequencing. *Molecular  
1089 Ecology Resources* e14094 (2025).
- 1090
- 1091 [21] Dean, F. B., Nelson, J. R., Giesler, T. L. & Lasken, R. S. Rapid amplification  
1092 of plasmid and phage DNA using Phi29 DNA polymerase and multiply-primed  
1093 rolling circle amplification. *Genome Research* **11**, 1095–1099 (2001).
- 1094
- 1095 [22] Lu, N., Qiao, Y., Lu, Z. & Tu, J. Chimera: The spoiler in multiple displacement  
1096 amplification. *Computational and Structural Biotechnology Journal* 1688–1696  
1097 (2023).
- 1098
- 1099 [23] Lu, N. *et al.* Exploration of whole genome amplification generated chimeric  
1100 sequences in long-read sequencing data. *Briefings in Bioinformatics* **24**, bbad275  
1101 (2023).
- 1102
- 1103 [24] Sedlazeck, F. J. *et al.* Accurate detection of complex structural variations using  
1104 single-molecule sequencing. *Nature Methods* 461–468 (2018).

- [25] Smolka, M. *et al.* Detection of mosaic and population-level structural variants with sniffles2. *Nature Biotechnology* 1571–1580 (2024). 1105  
1106  
1107
- [26] Chen, Y. *et al.* Deciphering the exact breakpoints of structural variations using long sequencing reads with DeBreak. *Nature Communications* 283 (2023). 1108  
1109  
1110
- [27] Heller, D. & Vingron, M. SVIM: Structural variant identification using mapped long reads. *Bioinformatics* 2907–2915 (2019). 1111  
1112  
1113  
1114  
1115
- [28] Jiang, T. *et al.* Long-read-based human genomic structural variation detection with cuteSV. *Genome Biology* 189 (2020). 1116  
1117  
1118
- [29] Alkan, C., Coe, B. P. & Eichler, E. E. Genome structural variation discovery and genotyping. *Nature Reviews Genetics* **12**, 363–376 (2011). 1119  
1120  
1121  
1122  
1123
- [30] Kiguchi, Y., Nishijima, S., Kumar, N., Hattori, M. & Suda, W. Long-read metagenomics of multiple displacement amplified DNA of low-biomass human gut phageomes by SACRA pre-processing chimeric reads. *DNA Research* **28**, dsab019 (2021). 1124  
1125  
1126
- [31] Kosugi, S. *et al.* Comprehensive evaluation of structural variation detection algorithms for whole genome sequencing. *Genome Biology* **20**, 117 (2019). 1127  
1128  
1129
- [32] Mahmoud, M. *et al.* Structural variant calling: The long and the short of it. *Genome Biology* **20**, 246 (2019). 1130  
1131
- [33] Dalla-Torre, H. *et al.* Nucleotide transformer: building and evaluating robust foundation models for human genomics. *Nature Methods* 287–297 (2025). 1132  
1133  
1134
- [34] Zhou, Z. *et al.* DNABERT-2: Efficient foundation model and benchmark for multi-species genomes, 1–24 (OpenReview.net, 2024). 1135  
1136  
1137
- [35] Nguyen, E. *et al.* HyenaDNA: Long-range genomic sequence modeling at single nucleotide resolution, Vol. 36, 43177–43201 (Curran Associates, Inc., 2023). 1138  
1139  
1140
- [36] Consens, M. E. *et al.* To transformers and beyond: Large language models for the genome (2023). [arXiv:2311.07621](https://arxiv.org/abs/2311.07621). 1141  
1142  
1143
- [37] Routhier, E. & Mozziconacci, J. Genomics enters the deep learning era. *PeerJ* **10**, e13613 (2022). 1144  
1145  
1146
- [38] Li, Y. *et al.* A genomic language model for chimera artifact detection in nanopore direct rna sequencing. *bioRxiv* (2024). URL <https://www.biorxiv.org/content/early/2024/10/25/2024.10.23.619929>. 1147  
1148  
1149  
1150

- 1151 [40] PLC., O. N. Dorado. <https://github.com/nanoporetech/dorado> (2023).  
1152  
1153 [41] Martin, M. Cutadapt removes adapter sequences from high-throughput sequencing reads. *Embojournal* **17**, 10–12 (2011).  
1154  
1155 [42] Li, H. Minimap2: Pairwise alignment for nucleotide sequences. *Bioinformatics*  
1156 3094–3100 (2018).  
1157  
1158 [43] Danecek, P. *et al.* Twelve years of SAMtools and BCFtools. *GigaScience* giab008  
1159 (2021).  
1160  
1161 [44] De Coster, W. & Rademakers, R. NanoPack2: Population-scale evaluation of  
1162 long-read sequencing data. *Bioinformatics* **39**, btad311 (2023).  
1163  
1164 [45] Paszke, A. *et al.* *PyTorch: An imperative style, high-performance deep learning*  
1165 *library*, Vol. 32, 8024–8035 (Curran Associates, Inc., 2019).  
1166  
1167 [46] Falcon, W. & The PyTorch Lightning team. PyTorch Lightning. GitHub  
1168 repository (2019). URL <https://github.com/Lightning-AI/lightning>.  
1169  
1170 [47] Loshchilov, I. & Hutter, F. *Decoupled weight decay regularization* (2019).  
1171  
1172 [48] Yadan, O. Hydra - a framework for elegantly configuring complex applications.  
1173 GitHub repository (2019). URL <https://github.com/facebookresearch/hydra>.  
1174  
1175 [49] Chen, X. *et al.* Manta: Rapid detection of structural variants and indels for  
1176 germline and cancer sequencing applications. *Bioinformatics* 1220–1222 (2016).  
1177  
1178 [50] Rausch, T. *et al.* DELLY: Structural variant discovery by integrated paired-end  
1179 and split-read analysis. *Bioinformatics* i333–i339 (2012).  
1180  
1181 [51] Wala, J. A. *et al.* SvABA: Genome-wide detection of structural variants and  
1182 indels by local assembly. *Genome Research* 581–591 (2018).  
1183  
1184 [52] Guo, Q., Li, Y., Wang, T.-Y., Ramakrishnan, A. & Yang, R. OctopusV and  
1185 TentacleSV: A one-stop toolkit for multi-sample, cross-platform structural variant  
1186 comparison and analysis. *Bioinformatics* btaf599 (2025).  
1187  
1188 [53] English, A. C., Menon, V. K., Gibbs, R. A., Metcalf, G. A. & Sedlazeck, F. J.  
1189 Truvari: Refined structural variant comparison preserves allelic diversity. *Genome*  
1190 *Biology* **23**, 271 (2022).  
1191  
1192 [54] Virtanen, P. *et al.* SciPy 1.0: Fundamental algorithms for scientific computing in  
1193 python. *Nature Methods* 261–272 (2020).  
1194  
1195 [55] Hunter, J. D. Matplotlib: A 2d graphics environment. *Computing in Science &*  
1196 *Engineering* 90–95 (2007).

[56] Waskom, M. L.	seaborn: statistical data visualization.	<i>Journal of Open Source Software</i>	3021 (2021).	1197
				1198
				1199
				1200
				1201
				1202
				1203
				1204
				1205
				1206
				1207
				1208
				1209
				1210
				1211
				1212
				1213
				1214
				1215
				1216
				1217
				1218
				1219
				1220
				1221
				1222
				1223
				1224
				1225
				1226
				1227
				1228
				1229
				1230
				1231
				1232
				1233
				1234
				1235
				1236
				1237
				1238
				1239
				1240
				1241
				1242